Journal of Energy Storage 153 (2026) 121018

Contents lists available at ScienceDirect

Journal of Energy Storage

journal homepage: www.elsevier.com/locate/est

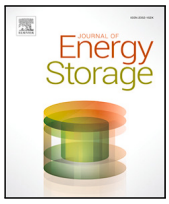

Research Papers

Fuzzy logic–based estimation and topological ordering of pack-to-pack capacity variations in parallel-connected batteries

Susann Wunsch [a,b,*], Natalia A. Cañas [a], Eric Sax [b]

[a] Daimler Buses, Hanns-Martin-Schleyer-Straße 21-57, Mannheim, 68305, Germany
[b] Karlsruhe Institute of Technology, ITIV, Engesserstr. 5, Karlsruhe, 76131, Germany

ARTICLE INFO

Keywords:
Battery health
Capacity difference
State of Health (SOH)
Electric vehicle
Lithium-ion batteries
Fuzzy logic
Topological ordering

ABSTRACT

Reliable estimation of the State of Health (SOH) remains a key challenge for battery systems, as many established approaches rely on detailed battery models and aging-dependent parameters. In industrial applications, SOH values are often delivered by proprietary algorithms, motivating the need for independent cross-checking from the customer's perspective. This work proposes a model-free method to infer relative capacity differences between parallel-connected battery packs using only measured current and voltage signals. Three probabilistic distributions derived from standard operational data are combined via a fuzzy logic-based pairwise comparison, and the resulting relations are aggregated into a global capacity ranking using topological ordering. The method requires neither battery modeling nor knowledge of absolute capacities and provides a logically consistent relative reference for SOH validation. Simulation studies show that the true capacity order is correctly identified across multiple load profiles, with increased uncertainty when higher-capacity packs simultaneously exhibit higher internal resistance. The approach is further validated using 26 months of real-world data from an electric city bus with five parallel-connected NMC battery packs, capturing evolving capacity differences, including a known pack replacement. The results show substantial agreement with a Kalman filter-based SOH estimation for most pack pairs, while also revealing cases of disagreement and delayed adaptation. The proposed method provides a scalable and transparent cross-check for SOH algorithms, enabling probabilistic validation of relative capacity estimates in multi-pack battery systems.

1. Introduction

With the growing commercialization of electric mobility and the increased usage of stationary storage systems to buffer renewable energy generation, batteries are expected to demonstrate high reliability and long-lasting performance. However, achieving these objectives is fundamentally challenged by continuous aging processes, which progressively affect the ability of a battery to deliver energy and power over time.

In lithium-ion batteries, aging results from various interacting processes, leading to a loss of active material and cyclable lithium ions, which gradually degrades the battery's performance, as investigated in several studies, for example in [1–4]. The most perceptible macroscopic consequences of aging are an increase in internal resistance and a decrease in capacity. Both serve as key indicators for assessing the battery's State of Health (SOH). In this work, SOH is defined in terms of capacity, i.e., the ratio of the currently available maximum physical capacity to the nominal capacity at Begin of Life (BOL).

Accurate on-board estimation of the SOH is essential for reliable battery system operation, including the prediction of remaining range and determination of the battery's end of life (EOL). Advanced approaches, such as Kalman filter-based methods, are either applied primarily for State of Charge (SOC) estimation, serving as a basis for subsequent SOH estimation, or in dual configurations estimating both SOC and SOH simultaneously. These approaches provide high accuracy but generally depend on detailed battery parameter knowledge, as applied in [5–8]. Since these parameters change with ongoing aging, model-based approaches lose precision over time. Moreover, many SOH estimation algorithms are calibrated for specific operating windows and achieve their best accuracy when the battery regularly undergoes conditions such as high depths of discharge. This limits practical applicability and can reduce the estimation robustness. In addition, in commercial battery systems, SOH values are often obtained from externally developed, proprietary algorithms that lack transparency and their validation requires high effort.

* Corresponding author at: Karlsruhe Institute of Technology, ITIV, Engesserstr. 5, Karlsruhe, 76131, Germany.
E-mail addresses: susann.wunsch@daimlertruck.com (S. Wunsch), natalia.canas@daimlertruck.com (N.A. Cañas), eric.sax@kit.edu (E. Sax).

https://doi.org/10.1016/j.est.2026.121018
Received 14 October 2025; Received in revised form 19 January 2026; Accepted 6 February 2026
Available online 11 February 2026

To address these challenges, this work introduces a probabilistic ranking method for capacities, and consequently SOHs, of parallel-connected battery packs. The approach applies a fuzzy logic-based pairwise comparison (Section 2.2), relying solely on distributions of measured signals, namely voltage and current (Section 2.1). The pairwise comparisons are subsequently combined to derive a global capacity order across all interconnected battery packs using topological sorting (Section 2.3). The resulting ordering provides a relative proxy ground truth for SOH estimates, independent of the underlying algorithm.

The main contributions and advantages of the proposed method can be summarized as follows:

- *Model-free relative capacity assessment:* The method infers pairwise capacity relations without requiring explicit battery models, OCV parameterization, or prior knowledge of internal resistances, relying solely on measured voltage and current signals.
- *Probabilistic SOH plausibility check:* It provides an algorithm-independent, relative reference for plausibilizing SOH estimates in systems with parallel-connected battery packs, rather than an absolute SOH value.
- *Distribution-based inference under real operation:* Capacity relations are derived from statistical patterns across multiple operating phases, enabling inference under realistic load profiles without requiring dedicated test cycles.
- *Scalable comparison framework:* Pairwise capacity relations are aggregated into a global ranking, with larger numbers of parallel packs improving robustness through mutual consistency checks.
- *Explicit handling of uncertainty:* The fuzzy logic formulation maps agreement and contradiction between multiple input distributions to graded confidence levels, making uncertainty an integral part of the output rather than a byproduct.

Since the method requires no prior knowledge of capacities or detailed battery modeling, it complements conventional SOH algorithms and increases confidence in SOH estimation results.

Recent research increasingly treats cell-to-cell inconsistency as an inherent feature of state estimation rather than as a disturbance. Examples include reformulated pack models based on inverse dynamics, which resolve algebraic loops and preserve observability in parallel configurations [9], and descriptor system theory, which enables scalable observers for individual cell SOCs using only aggregated current and voltage measurements [10]. Other contributions embed inconsistency directly at the module level to enhance numerical robustness in SOC estimation [11] or integrate online inconsistency metrics for real-time monitoring of SOC divergence [12]. Another approach jointly estimates inconsistency and SOH from fast-charging features using Gaussian-process regression, showing that inconsistency reflects aging and improves prediction accuracy [13]. Together, these methods enable practical and scalable estimation under heterogeneity; however, they rely on detailed knowledge of individual cell characteristics to capture inconsistencies and provide only limited internal plausibility checks for the estimated state.

Fuzzy logic has been applied to enhance estimation robustness under uncertainty and inconsistency. Hybrid fuzzy Kalman approaches address inconsistency in parallel packs for SOC estimation [14], whereas earlier work applied fuzzy logic to SOH [15] or SOC estimation [16] without considering pack inconsistency. Beyond the battery domain, fuzzy systems have also been successfully used in areas such as driver monitoring and collision warning [17,18], highlighting their suitability for adaptive decision-making under uncertainty. These methods offer practical adaptability and improved robustness, but require careful rule tuning.

Research on capacity variation and its development over time shows that intrinsic cell-to-cell variability plays a key role in pack modeling [19]. Initial differences in capacity and resistance influence aging patterns and contribute to divergence within packs [20,21], while studies on parallel-connected cells and modules demonstrate how inhomogeneity evolves with cycling and depends on pack architecture [22,23]. Collectively, these studies view cell-to-cell variation as a stochastic, time-evolving property reflected in pack-level statistics while considering individual cell and module dynamics.

Overall, prior work has primarily addressed inconsistency in SOC estimation, with some extensions to parameters and SOH. Studies of capacity and resistance variation link these parameters to unequal current distribution, accelerated aging, and long-term divergence, while fuzzy logic has been applied to improve robustness in SOC and, to a lesser extent, SOC–SOH estimation. However, no approach derives relative capacity differences directly from standard battery signals or establishes a probabilistic capacity ordering. The proposed method fills this gap by exploiting inherent comparison opportunities in parallel-connected packs, where physical interactions and logical constraints expose relative capacities and provide a novel plausibility reference for SOH algorithms.

2. Theory and calculation

2.1. Measurement distributions

The internal resistance and capacity of a battery, both indicative of its aging state, manifest in various measurable signals. Resistance directly influences the current distribution among parallel-connected packs, while capacity is inferred indirectly from differences in open-circuit voltage (OCV). The following section derives three distributions, (D1)-(D3), from the variation of selected measurable quantities across parallel-connected batteries. [24]

The current of a battery i_1 within a parallel connection of n batteries can be expressed as a function of the total current applied to the circuit (Eq. (1)). The equation assumes stationary conditions, meaning that the batteries immediately reach their equilibrium voltages.

$$i_1 = \frac{i_{total}}{R_1 \sum_{k=1}^{n} 1/R_k} + \frac{\sum_{k=1}^{n} (OCV_1 - OCV_k)/R_k}{R_1 \sum_{k=1}^{n} 1/R_k} \tag{1}$$

The current distribution depends not only on the total current but also on the open-circuit voltages (OCV) and internal resistances (R) of the connected batteries. In the given form, the equation consists of two additive terms. The first term is proportional to the total current and is determined solely by the ratio between the resistance of the battery considered and the resistances of the remaining batteries. The second term is independent of the total current and represents a correction based on OCV differences between the battery considered and the others, weighted by the same resistance ratio. At *high total currents*, the first term dominates, making the resistance ratio the primary determinant of the current distribution. At *low total currents*, the first term becomes negligible and OCV differences dominate. If the total current is zero, only an OCV difference can drive current between batteries.

This relationship enables the current distribution to serve as an implicit indicator of two battery characteristics: resistance variance, which dominates the distribution during phases of high total current (D1), and OCV variance, which defines the distribution during phases of low total current (D2). As resistance is also influenced by temperature and SOC, the observed pack-to-pack differences in (D1) cannot be attributed solely to aging.

The open-circuit voltage (OCV) is influenced not only by resistance-related inhomogeneities in current distribution but also by capacity variations among the batteries. The SOC can be calculated by recursively integrating the charged and discharged ampere-hours, accounting for the coulombic efficiency η, and scaling the result by the total capacity Q (Eq. (2)). This equation establishes the link between SOC and capacity; however, since SOC is not a directly measurable quantity, its relationship to OCV must be utilized. In general, a higher SOC corresponds to a higher OCV, with the sensitivity of this relationship determined by the cell chemistry. The sensitivity can be increased by analyzing the OCV/SOC curve and focusing on its steeper regions.

$$SOC(t_2) = SOC(t_1) - 1/Q \int_{t_1}^{t_2} \eta(t) i(t)\, dt \tag{2}$$

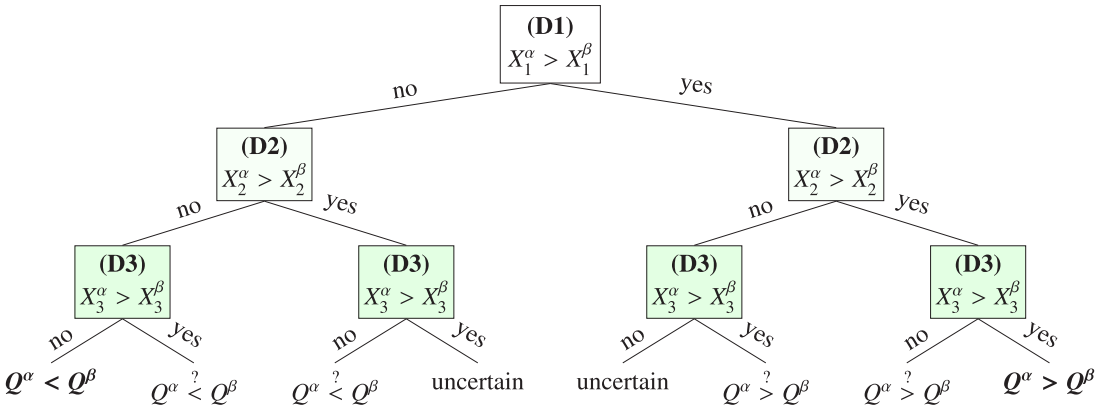

Fig. 1. Decision tree for associating the differences in the measured distributions with capacity differences between pack α and pack β.

Eq. (2) further implies that, under identical current conditions, batteries with higher capacities will exhibit higher OCVs during discharge and lower OCVs during charge compared to lower-capacity batteries. Based on this observation, the third distribution (D3) is defined as the voltage measured on rested battery packs after they have been simultaneously disconnected from the DC link, following a period of predominantly unidirectional current flow (either charging or discharging). This behavior is inherently non-linear and self-coupled, as the distribution of the total current in a parallel-connected circuit is affected by the OCV variations themselves, thereby invalidating the assumption of identical currents across all branches.

In summary, three distributions are relevant for the capacity difference analysis:

- **(D1)** Current distribution X_1 during high-current phases, reflecting resistance variation
- **(D2)** Current distribution X_2 during low-current phases, reflecting OCV variation
- **(D3)** Voltage distribution X_3 after simultaneous disconnection from the DC link, reflecting OCV variation

When jointly considering the three distributions, the relative capacity relationship of two packs can be inferred (Fig. 1). The reasoning follows a concessive syllogism with the observed differences in (D1) serving as a consistency prior. First, if pack α exhibits systematically higher currents in (D1) than pack β, then, independent of the specific physical cause of this imbalance and without invoking capacity differences, pack α is expected to reach lower OCVs during discharging and higher OCVs during charging, solely due to the resistance-based current variation. However, if despite this expectation pack α consistently shows higher OCVs during discharge and lower OCVs during charging in (D2) and (D3), the OCV difference cannot be attributed to resistance effects alone. This pattern logically implies a higher capacity of pack α relative to pack β (and vice versa). These two syllogistic conclusions are represented by the outer branches of the decision tree in Fig. 1.

Since both distributions, (D2) and (D3), provide information on OCV differences, they can be cross-validated to increase confidence in the conclusion if they show consistent results. In cases of disagreement, the individual deltas and the statistical significance of each distribution, determined by the total number of samples and the standard deviation, should be used to assess their respective reliability (Section 2.2).

If no contraindications exist between (D1) and (D2) or (D3), respectively, the capacity difference estimation has the highest uncertainty, since the influence of capacity on the OCV cannot be distinctly separated from the effects of varying pack currents, regardless of whether these current differences originate from aging, temperature, or SOC variations. These cases are represented by the inner structure of the decision tree.

2.2. Fuzzy logic for capacity difference estimation

To estimate the relative capacity differences between two battery packs, a fuzzy-logic-based approach is proposed. This method does not require training data; instead, it infers the output probability directly from known distribution implications and their interrelations (Section 2.1). The approach combines the relative differences of the measured input distributions (D1)–(D3) to produce a probabilistic output that quantifies the likelihood of the first pack having a higher or lower capacity than the second pack. The underlying heuristic enables the integration of domain knowledge into the probabilistic reasoning.

As a first step, unique dual combinations of the available interconnected battery packs α and β are defined. For each combination, the difference between the distributions of both packs is computed for each distribution type X_i. This results in three input distributions per combination, representing the pack-to-pack differences of the originally defined distributions, denoted as $X_i^{(\alpha,\beta)}$ with individual lengths of n_i samples. For each of these, the probability density function $\hat{f}_i(x)$ is estimated using Kernel Density Estimation with a Gaussian kernel $K(u)$, with the bandwidth h determined according to Scott's rule (Eq. (3a)–(3b)).

$$\hat{f}_i(x) = \frac{1}{n_i h} \sum_{k=1}^{n_i} K\left(\frac{x - x_k}{h}\right) \tag{3a}$$

$$K(u) = \frac{1}{\sqrt{2\pi}} \exp\left(-\frac{u^2}{2}\right) \tag{3b}$$

The fuzzy system is based on two primary fuzzy sets $A_{i,j} \in \{A_{pos}, A_{neg}\}$. The degrees of membership, denoted as the membership functions $\mu^{A_{i,j}} \in \{\mu_i^{pos}, \mu_i^{neg}\}$, are derived from the distribution function $\hat{f}_i(x)$. Here, μ_i^{pos} corresponds to the integral over its positive area, determined by p_i, while μ_i^{neg} corresponds to the integral over its negative area. Consequently, A_{pos} represents the positive and A_{neg} the negative differences in $X_i^{(\alpha,\beta)}$ (Eq. (4a)–(4c)).

$$p_i = P(X_i^{(\alpha,\beta)} > 0) = \int_0^\infty \hat{f}_i(x)\, dx \tag{4a}$$

$$A_{i,j} \subset X_i^{(\alpha,\beta)}, \quad \mu^{A_{i,j}} : X_i^{(\alpha,\beta)} \to [0,1],$$
$$p_i \in A_{i,j} \iff \mu^{A_{i,j}}(p_i) > 0 \tag{4b}$$

$$\mu_i^{pos} = p_i; \quad \mu_i^{neg} = 1 - \mu_i^{pos} \tag{4c}$$

Special attention is given to decision paths that lead to highly uncertain states (Fig. 1). To address this, four fuzzy subsets are introduced by dividing each primary fuzzy set into two sub-ranges. The corresponding membership functions $\mu^{A_{i,j}} \in \{\mu_i^{\text{pos,high}}, \mu_i^{\text{pos,low}}, \mu_i^{\text{neg,high}}, \mu_i^{\text{neg,low}}\}$ are defined using rising and falling ramp functions

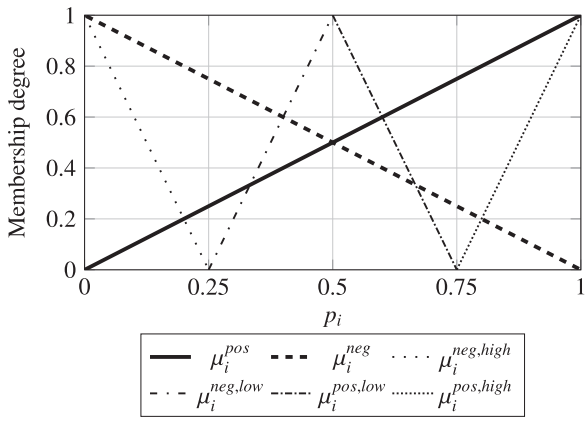

Fig. 2. Membership degrees as a function of p_i for all input membership functions μ_i.

(Eq. (5a)–(5d)), ensuring that the degree of membership increases monotonically within the respective sub-range, while values outside the defined sub-range are clipped to zero (Fig. 2). The central threshold at $p_i = 0.5$ has a direct semantic interpretation, separating ambiguous cases from those with a dominant direction, while the additional subdivision at $p_i = 0.75$ (and symmetrically at $p_i = 0.25$) refines each primary fuzzy set into weak and strong evidence. This symmetric design enables the rule base to distinguish confidence levels in an interpretable manner without introducing additional heuristic assumptions.

These subsets are subsequently employed in the fuzzy rule base, assigning greater weight to combinations of the three input distributions that remain close to the more certain capacity-implication paths. In this way, the fuzzy system reduces convergence toward highly uncertain outcomes in the capacity comparison.

$$R(p;a,b) = \begin{cases} 0, & p < a, \\ \dfrac{p-a}{b-a}, & a \le p \le b, \\ 0, & p > b, \end{cases} \tag{5a}$$

$$F(p;a,b) = \begin{cases} 0, & p < a, \\ \dfrac{b-p}{b-a}, & a \le p \le b, \\ 0, & p > b, \end{cases} \tag{5b}$$

$$\mu_i^{\text{pos,high}} = R(p_i;0.75,1); \quad \mu_i^{\text{pos,low}} = F(p_i;0.5,0.75) \tag{5c}$$

$$\mu_i^{\text{neg,high}} = F(p_i;0,0.25); \quad \mu_i^{\text{neg,low}} = R(p_i;0.25,0.5) \tag{5d}$$

The fuzzy system employs a functional consequent design of the Sugeno type. In the general formulation of the fuzzy rules, the output of rule j is expressed as a function of the indirect inputs p_i (Eq. (6)). This eliminates the need to explicitly define fuzzy output sets; instead, the output can be expressed directly as a function of the inputs, which allows heuristic reasoning about input–output relations to be incorporated in a mathematically consistent way. This is particularly appropriate in the present case, as both the inputs and the output are distribution-based probabilistic quantities and can thus be consistently combined. As the system represents a static mapping from input to output, without temporal feedback or adaptive parameters, each evaluation is independent and requires no consideration of convergence.

$$\begin{aligned} R_j: \quad & IF \quad X_1^{(\alpha,\beta)} \in A_{1,j} \quad AND \quad X_2^{(\alpha,\beta)} \in A_{2,j} \\ & AND \quad X_3^{(\alpha,\beta)} \in A_{3,j} \quad THEN \quad p_y^{(R_j)} = f(p_1,p_2,p_3) \end{aligned} \tag{6}$$

Table 1
Overview of fuzzy rules.

Rule R_j	Input $X_1^{(\alpha,\beta)}$		Input $X_2^{(\alpha,\beta)}$		Input $X_3^{(\alpha,\beta)}$	
	$A_{1,j}$	$[a_{1,j}, b_{1,j}]$	$A_{2,j}$	$[a_{2,j}, b_{2,j}]$	$A_{3,j}$	$[a_{3,j}, b_{3,j}]$
R_1			A_{pos}	$[s/2, s]$	A_{pos}	$[s/2, s]$
R_2	A_{pos}	$[s/2, 2]$	A_{neg}	$[-s/2, s/2]$	A_{pos}	$[s/2, s]$
R_3			A_{pos}	$[s/2, s]$	A_{neg}	$[-s/2, s/2]$
R_4	A_{pos}	$[0, 0]$	A_{neg}	$[0, 0]$	A_{neg}	$[0, 0]$
R_5	$A_{pos,high}$	$[s/2, s]$	$A_{neg,low}$	$[-s/2, s/2]$	$A_{neg,low}$	$[-s/2, s/2]$
R_6	$A_{pos,low}$	$[-s/2, s/2]$	$A_{neg,high}$	$[-s, -s/2]$	$A_{neg,high}$	$[-s, -s/2]$
R_7			A_{neg}	$[-s, -s/2]$	A_{neg}	$[-s, -s/2]$
R_8	A_{neg}	$[-s, -s/2]$	A_{neg}	$[-s, -s/2]$	A_{pos}	$[-s/2, s/2]$
R_9			A_{pos}	$[-s/2, s/2]$	A_{neg}	$[-s, -s/2]$
R_{10}	A_{neg}	$[0, 0]$	A_{pos}	$[0, 0]$	A_{pos}	$[0, 0]$
R_{11}	$A_{neg,high}$	$[-s, -s/2]$	$A_{pos,low}$	$[-s/2, s/2]$	$A_{pos,low}$	$[-s/2, s/2]$
R_{12}	$A_{neg,low}$	$[-s/2, s/2]$	$A_{pos,high}$	$[s/2, s]$	$A_{pos,high}$	$[s/2, s]$

For simplicity, the output function of the rules is defined solely in terms of the integral over the positive area of the input distributions, denoted as p_i, since all other memberships are derived from this quantity. The function polarizes p_i to the interval $[-s, s]$, with s as a scaling factor, to improve interpretability and visualization. Subsequently, the polarized value is rescaled, depending on the specific rule content, to a new interval $[a_{i,j}, b_{i,j}]$ (Eq. (7a)–(7b)).

$$\begin{aligned} & p_i \in [0,1] \;\mapsto\; p_{i,\text{pol}} = s(2p_i - 1) \in [-s, s] \\ & \;\mapsto\; p_{i,\text{scaled}} = f(p_{i,\text{pol}}) \in [a_{i,j}, b_{i,j}] \subset \mathbb{R} \end{aligned} \tag{7a}$$

$$\text{for } s = 1: \quad f: [-1,1] \to [a_{i,j}, b_{i,j}] \tag{7b}$$

In total, twelve rules are defined. Depending on the conjunction of different fuzzy sets, a specific scaling interval is applied as a function of the scaling factor s (Table 1). The rule definition follows the structure of the decision tree (Fig. 1): Rules R_1 to R_6 correspond to the right branch of the tree (positive decision for (D1)), while the rules R_7 to R_{12} correspond to the left branch. The first rules (R_1 and R_7) capture the outer branches, which represent decision paths with strong capacity implications. The subsequent pairs of rules (R_2, R_3 and R_7, R_8) represent cases where the two OCV-based distributions (D2) and (D3) contradict each other in their implications for the OCV difference, thereby introducing higher uncertainty into the capacity comparison. Finally, the remaining rule subsets (R_4, R_5, R_6 and R_{10}, R_{11}, R_{12}) address the two inner uncertain paths of the decision tree. They both direct the output toward zero and integrate the four fuzzy subsets.

The scaling intervals map input distributions $X_i^{(\alpha,\beta)}$ of identical sign to the outer regions of the output interval $[-s, s]$, while contradictory distributions are rescaled toward the center. This allows small deviations between agreeing distributions ((D1) & (D2) or (D1) & (D3)) to act as minor amplifications of their joint tendency, whereas larger deviations can still pull the output in the opposite direction. The subdivision of the output interval into $[-s, -s/2, 0, s/2, s]$ follows directly from the decision-tree logic: the outer intervals represent strong and consistent evidence for a capacity difference, while the inner intervals correspond to partially conflicting or weaker indications. The symmetric half-step spacing ensures equidistant transitions between semantic confidence levels and results in monotonic output behavior with proportional scaling as agreement among the input distributions increases.

To reduce uncertain outputs, the fuzzy subsets are defined such that a high membership of the (D1)-based or the (D2)/(D3)-based distributions to the positive or negative set compensates small contrary inputs. The procedure reflects that sign agreement provides evidence for a specific capacity relation, while disagreement indicates uncertainty rather than the opposite relation. However, by quantitatively evaluating positive and negative differences within the distributions, a tendency can still be inferred, allowing the system to assign higher likelihoods to certain outcomes.

Overall, the fuzzy parameters were selected to explicitly encode the qualitative decision logic of the method in a transparent and interpretable form, rather than to achieve numerical optimality for a specific dataset. Moderate variations of the thresholds primarily affect the confidence of the output but rarely its sign, as the inference relies on relative agreement and contradiction patterns across the three distributions.

The transformed probabilities $p_{i,\text{scaled}}$ are aggregated into a weighted average to account for the statistical relevance of the OCV-based input distributions $X_{2,3}^{(\alpha,\beta)}$ (Eq. (8a)–(8b)). For (D1) ($i = 1$), the weight is fixed at $w_1 = 1$. For (D2) and (D3) ($i = 2, 3$), the weights are computed as relative contributions based on the standard deviations σ_i and sample sizes n_i. To ensure comparability between different physical units, $X_{2,3}^{(\alpha,\beta)}$ are scaled to their minimum and maximum before computing σ_i. Root functions are applied to the weights to adjust the strong imbalance in sample counts between (D2) and (D3), which arises naturally from their definitions. In the analyzed city bus dataset (Section 4.2) a typical ratio of $n_2/n_3 \gtrsim 100$ is observed; this value may vary for other vehicles or operating scenarios, while the qualitative imbalance between (D2) and (D3) remains inherent to the monitoring logic.

$$w_i = \frac{\sqrt[3]{n_i}/\sqrt{\sigma_i}}{\sum_{k=2}^{3} \sqrt[3]{n_k}/\sqrt{\sigma_k}}, \quad i = 2, 3 \tag{8a}$$

$$p_y^{(R_j)} = \frac{\sum_i w_i p_{i,\text{scaled}}}{\sum_i w_i} \tag{8b}$$

As the fuzzy rules are formulated as conjunctions between the inputs, the firing strength $\mu^{(R_j)}$ of each rule is defined as the minimal degree of membership among all inputs with respect to their corresponding sets (Eq. (9)). With this value, the activation level of the rule is determined.

$$\mu^{(R_j)} = \min_i(\mu^{A_{i,j}}) \tag{9}$$

Defuzzification is not required, as the output in a Sugeno fuzzy system is already scalar. The overall output is computed as the weighted average of the rule outputs $p_y^{(R_j)}$, where the weights correspond to the firing strengths $\mu^{(R_j)}$ (Eq. (10)). The aggregated output $P_Y^{(\alpha,\beta)} \in [-s, s]$ quantifies the inferred capacity relation between pack α and pack β. A value of $P_Y^{(\alpha,\beta)}$ approaching s indicates high certainty that pack α has a higher capacity than pack β, while values approaching $-s$ imply the opposite ($Q_\alpha < Q_\beta$). Outputs close to zero reflect a high uncertainty regarding the capacity relation.

$$P_Y^{(\alpha,\beta)} = \frac{\sum_j \mu^{(R_j)} p_y^{(R_j)}}{\sum_j \mu^{(R_j)}} \tag{10}$$

For visualization purpose, the fuzzy rules are parametrized with $s = 1$ and identical weightings $w_{2,3} = 0.5$ are assumed for the OCV-based distributions. Hence the output $P_Y^{(\alpha,\beta)}$ can be represented as isosurfaces of constant values of $\mu_1^{pos} \in \{0, 0.1, 0.2, \ldots, 0.9, 1\}$ expressed as functions of μ_2^{pos} and μ_3^{pos}, whereby the complementary relation $\mu_i^{neg} = 1 - \mu_i^{pos}$ applies (Fig. 3). The subset-related rules lead to more pronounced concave surfaces in the central region as $X_1^{(\alpha,\beta)}$ becomes more negative ($\mu_1^{pos} \to 0$), and to more pronounced convex surfaces as $X_1^{(\alpha,\beta)}$ increases ($\mu_1^{pos} \to 1$).

2.3. Topological ordering of pack capacities

The quantification of pack capacity relations, determined in Section 2.2, derives a bilateral comparison between pairs of battery packs. This set of pairwise logical connections can subsequently be utilized to construct a global ordering of capacities across all parallel-connected battery packs.

In graph theory, a topological ordering provides a way to arrange the vertices of a directed graph according to its dependencies. Let $G = (V, E)$ be a finite directed acyclic graph (DAG), where V is the set of vertices and $E \subseteq V \times V$ is the set of directed edges. A topological ordering π of G is defined as a bijection (Eq. (11)), so that for every edge $(v_i, v_j) \in E$ the ordering condition $\pi(v_i) < \pi(v_j)$ is satisfied.

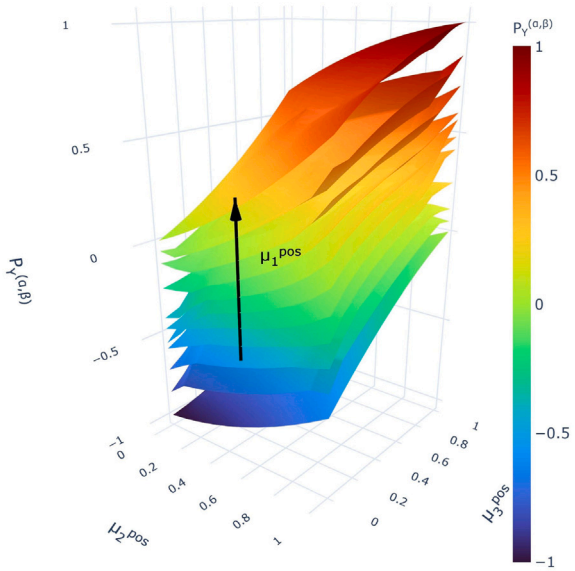

Fig. 3. Visualization of fuzzy rules output: $P_Y^{(\alpha,\beta)}$ as a function of μ_i^{pos}.

$$\pi : V \to \{1, 2, \ldots, |V|\} \tag{11}$$

Such an ordering exists if G contains no directed cycles (Eq. (12)).

$$\neg\exists\, v_1, \ldots, v_k \in V,\ k \geq 2 : \quad (v_1, v_2), (v_2, v_3), \ldots, (v_k, v_1) \in E \tag{12}$$

The topological order π can be viewed as a linear extension of the partial order $\prec$ on V, where $v_i \prec v_j$ applies, if a directed path from v_i to v_j in G exists. This implies the consistency property (Eq. (13)).

$$v_i \prec v_j \implies \pi(v_i) < \pi(v_j), \quad \forall\, v_i, v_j \in V. \tag{13}$$

Each battery pack capacity is represented as a vertex in the set V, whereby the ordering of vertices is determined by the bilateral capacity comparison between pack α and pack β, denoted by $P_Y^{(\alpha,\beta)}$ (Eq. (14a)–(14b)).

$$P_Y^{(\alpha,\beta)} < 0 \implies Q_\alpha \prec Q_\beta \tag{14a}$$

$$P_Y^{(\alpha,\beta)} > 0 \implies Q_\beta \prec Q_\alpha \tag{14b}$$

If $P_Y^{(\alpha,\beta)} = 0$, no evidence of a capacity difference could be established, and the corresponding packs appear as independent vertices.

The adjacency matrix $A \in \{0, 1\}^{|V|\times|V|}$ encodes the directed pairwise capacity relations of the directed graph $G = (V, E)$ (Eq. (15)), while the in-degree $\deg^-(v_j)$ of a vertex v_j quantifies the number of strictly smaller capacities preceding it in the induced partial order (Eq. (16)).

$$A_{ij} = \begin{cases} 1, & (v_i, v_j) \in E, \\ 0, & \text{otherwise}, \end{cases} \tag{15}$$

$$\deg^-(v_j) = \sum_{i=1}^{|V|} A_{ij}, \tag{16}$$

Linear extensions are constructed using Kahn's topological sorting algorithm:

1. Initialize an empty ordered list L and $S = \{v \in V \mid \deg^-(v) = 0\}$.
2. While $S \neq \emptyset$:
   (a) Select and remove $v \in S$, append v to L.

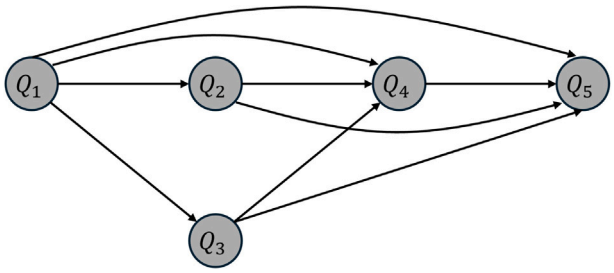

Fig. 4. Exemplary directed acyclic graph (DAG) for battery pack capacities.

(b) For each $(v_i, v_j) \in E$, remove the edge (set $A_{ij} = 0$).
(c) Insert v_j into S if $\deg^-(v_j) = 0$.

3. If nonzero entries remain in the adjacency matrix **A** after termination, the graph contains a directed cycle; otherwise, L is a valid topological order.

This cycle check serves as a consistency test for the estimated pairwise relations $P_Y^{(\alpha,\beta)}$. If no cycles are detected, different choices of vertices from S provide distinct valid orderings, such that all algorithm executions correspond to the linear extensions of this partial order. The number of such linear extensions increases with the number of independent vertices.

Fig. 4 illustrates an exemplary DAG of five pack capacities. In this case only $P_Y^{(2,3)}$ equals zero (connections exist between every other vertex), thus two consistent sequences are possible: the capacities of packs 2 and 3 can occupy either the second or third position in the ordering (Eq. (17a)–(17b)).

$$\pi(Q_1) < \pi(Q_2) < \pi(Q_3) < \pi(Q_4) < \pi(Q_5) \tag{17a}$$

$$\pi(Q_1) < \pi(Q_3) < \pi(Q_2) < \pi(Q_4) < \pi(Q_5) \tag{17b}$$

3. Materials and methods

The present study investigates simulated (Section 4.1) and real-world data (Section 4.2). For both cases, identical monitoring conditions for the input distributions apply:

(D1) Currents are recorded during high-current phases, corresponding to the top 5% of all current values over the monitored period ($|i_{pack,mean}| \gtrsim 70$ A).
(D2) Currents are recorded during low-current phases, corresponding to the bottom 15% of all current values over the monitored period ($|i_{pack,mean}| \lesssim 2$ A) . A higher percentage than in (D1) is required, as otherwise the monitored intervals would be dominated by extended rest phases.
(D3) Voltages are recorded at the end of an inactive period, provided that the battery packs are disconnected from the DC link for at least 10 s and that, during the preceding 30 min, the current direction corresponded to at least 80% charging or discharging activity. To increase the number of measurable events and thus the statistical significance in real-world data, the strict requirement of a fully equilibrated battery state is omitted; however, these short pauses provide a pragmatic approximation of relative OCV differences.

While calculating the distributions, the current direction was systematically incorporated so that variations in voltage and current were preserved rather than compensating each other.

The simulation results shall demonstrate the general feasibility of the method using known pack parameters and randomly selected load profiles from the real-world data set of Section 4.2. Battery currents and voltages were generated with a Thevenin model for each high-voltage battery (HVB), employing artificially defined capacities Q and ohmic resistances R_0 in a 5p configuration (Table 2). The parameter sets were selected to represent different comparison scenarios: a positive correlation (HVBs 4,5 and 1,2) and a negative correlation between capacity and resistance for the remaining pairs, with one pair exhibiting only a small capacity difference of 1 Ah (HVBs 1,3).

Table 2
Thevenin model parameters for simulations.

HVB no.	Q/Ah	$R_0/mOhm$	$R_1/mOhm$	C_1/F
1	140	170	100	500
2	135	165	100	500
3	141	160	100	500
4	150	155	100	500
5	145	150	100	500

As a second step, field data from electric city bus (Mercedes-Benz eCitaro Solo) equipped with five parallel-connected NMC high-voltage battery packs is analyzed. The observation period spans over 26 months. The data is recorded continuously by the battery management system at a sampling rate of 10 Hz and is filtered prior to analysis for sensor artifacts and communication dropouts. The evaluations are performed at approximately biweekly intervals, with each assessment covering seven consecutive days. A 7-day window is processed only if it contains at least 24 h of valid operation, defined as periods in which the packs are connected to the DC link. This window length ensures sufficient samples for all input distributions, reflecting recurring weekly usage patterns in regular bus operation, while the biweekly update rate balances statistical robustness and temporal resolution. Each boxplot in Section 4.2 represents one 7-day window and is plotted at its mean day. In the second month, HVB 5 was replaced with a new pack. This replacement is of particular relevance, as it directly changes the relative capacity relationships among the monitored packs and thus provides an inherent reference point for validating the evaluation.

Each distribution serves as the basis for calculating the difference distributions $X_i^{(\alpha,\beta)}$ for every combination of pack pairs (α, β), at each point in time and for each distribution type i. These difference distributions form the input for the fuzzy-logic-based estimation of capacity differences, as described in Section 2.2. With five packs under consideration, this results in ten distinct pack pairs. For the fuzzy rules, the parameter $s = 1$ is chosen, which ensures that the output $P_Y^{(\alpha,\beta)}$ lies within the interval $[-1, 1]$.

The real-world data results are additionally compared with capacity estimates obtained from a proprietary algorithm that employs a Kalman filter-based approach with online model parameter estimation, which was applied offline to the data set.

4. Results

4.1. Simulations

According to Table 2, the true capacity order derived from the parameterization of the pack models is:

$$\pi(Q_2) < \pi(Q_1) < \pi(Q_3) < \pi(Q_5) < \pi(Q_4) \tag{18}$$

For clarity, the results are presented in two plots, each showing five pack pairs (Fig. 5). The true order is correctly predicted in three of the four load profiles; the third profile deviates, giving $\pi(Q_1) < \pi(Q_2) < \pi(Q_3) < \pi(Q_4) < \pi(Q_5)$. Uncertainty ($P_Y^{(\alpha,\beta)} \to 0$) is highest for pack pairs exhibiting higher resistance together with higher capacity ($P_{Y,mean}^{(2,1)} = -0.03$ and $P_{Y,mean}^{(5,4)} = -0.02$), as this configuration consistently follows the two innermost branches of the decision tree (Fig. 1). No unambiguous inference can be drawn, as the pack with higher current consumption in (D1), induced by lower resistance, already explains the

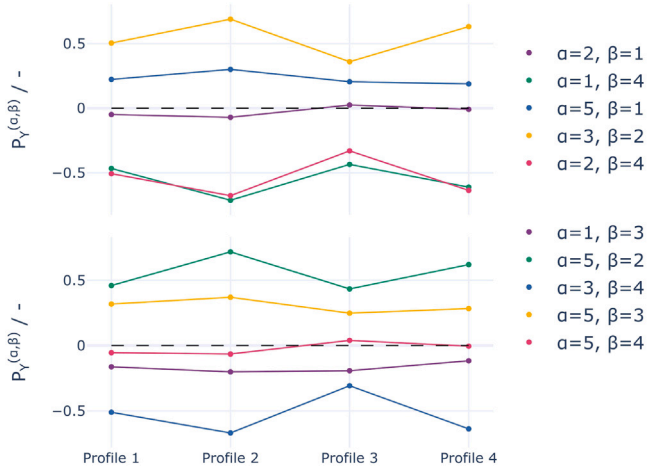

Fig. 5. $P_Y^{(\alpha,\beta)}$ for simulated load profiles.

lower OCV during discharge and higher OCV during charge, while the additionally lower capacity only reinforces this effect. This high level of uncertainty produces random noise around zero, which leads to the incorrectly predicted order for profile 3.

For pack pair (1,3), the uncertainty is also increased ($P_{Y,mean}^{(1,3)} = -0.17$) compared to the other pairs, as this pair exhibits a much smaller capacity difference, reducing the variations in (D2) and (D3).

4.2. Real-world data

To compare the development of the measured quantities, the deviations of the individual packs from the overall average are shown as boxplots over time. For clarity, statistical outliers outside the whiskers of the boxplots are not displayed. The mean values of the distributions are additionally represented as line plots for each pack.

Since distribution (D1) is strongly influenced by the absolute total current (Section 2.1), the deviations are calculated as a percentage of the absolute mean pack current. For (D2), where the effect of the total current is negligible, the deviations are shown directly as absolute values in amperes.

Input distribution. In (D1), HVBs 4 and 5 systematically consume and provide more current than the average, while HVBs 1-3 remain consistently below average (Fig. 6). This indicates lower internal resistances for HVBs 4 and 5.

In the second month after the start of monitoring, pack 5 was replaced by a new battery. This replacement caused a significant increase in current consumption and provision, driven by the lower resistance of the new pack. During the first four months after replacement, the current share of pack 5 decreased rapidly and then stabilized at a constant level.

The current distribution (D2) shows an almost inverted behavior compared to (D1): HVB 5 consumes and provides the least current, while HVB 1 shows the highest values (Fig. 7). This is expected, since packs with higher current in (D1) charge and discharge faster, reaching lower OCVs during discharge and higher OCVs during charging. In subsequent low-current phases, this results in reduced current flow as the other packs tend to equalize to the same OCV level.

The larger the deviation from the mean, the wider the boxplots appear, which reflects a broader distribution of the packs during the observed low-current phases. The deviation arises from its dependence on the OCV difference, which itself grows with the time available for divergence. As this time is not controlled, the dataset contains a broad range of different time spans, leading to higher variation.

The results of the voltage distribution (D3) are noisier, which is inherent to the monitoring logic and the consequently smaller number of observable situations (Fig. 8). However, certain trends can be identified. HVB 4 is mostly below the average voltage after discharging (and correspondingly above average after charging). This is consistent with the higher current share observed for HVB 4 in (D1). In contrast, HVB 2 and HVB 3 are mostly above average after discharging, which aligns with their generally smaller current shares in (D1). HVB 1 fluctuates more closely around the average level, but consumes and provides even less current than HVB 2 and HVB 3. This observation already provides an initial indication that HVB 1 may have a lower capacity.

Estimation results. A moving average was applied to smooth the raw output estimates (Fig. 9). For pack pairs involving HVB 5, the moving average was applied separately before and after the pack exchange. Following the simulation analysis in Section 4.1, outputs $|P_Y^{(\alpha,\beta)}| < 0.07$ are clipped to zero to exclude regions of high uncertainty.

The replacement of HVB 5 has a clearly visible impact on the results. For the pair $(5,4)$, shown in the lower plot, the outputs $P_Y^{(5,4)}$ are initially negative, indicating that the capacity of HVB 5 was lower than that of HVB 4. After the replacement, however, the output shifts to positive values, demonstrating that the new HVB 5 exhibits a higher capacity than HVB 4.

The topological ordering (Section 2.3) revealed no cycles, indicating consistency across all pairwise estimates (Fig. 10). The greater the number of pairwise estimates equal to zero, the more consistent orderings can be generated, and consequently the more ambiguous the ranking becomes. All possible ranks for each pack are shown as vertical lines; no preference is applied between multiple consistent orderings, and increased ambiguity is interpreted as reduced confidence rather than resolved into a single rank. Time periods in which, for one or more pack capacities, all combinations involving this pack result in $P_Y^{(\alpha,\beta)} = 0$ are omitted from the ordering to enhance the clarity of the visualization.

After the pack replacement, HVB 5 clearly occupies the highest ranks, whereas HVB 1 consistently appears at the lower ranks. For HVB 2 and HVB 4, the ranking is most ambiguous, as they occupy up to four different positions across various time spans.

SOH comparison. In a subsequent step, the pairwise results obtained from the fuzzy logic–based approach are compared with the SOH estimates generated by a Kalman filter using the same data set. Analogous to the presentation of the distribution plots (D1)–(D3) (Figs. 6–8), the pack SOHs are displayed as deviations from the mean SOH across all packs (Fig. 11). Following the pack replacement, HVB 5 is estimated to possess the highest capacity, followed by HVB 3. Approximately halfway through the observation period, the capacity of HVB 4 decreases below the capacities of HVBs 1 and 2. After replacing HVB 5, it can be observed that the Kalman filter requires several estimation steps to adapt and stabilize to the new SOH level. This delayed response is consistent with the recursive nature of the estimator, which relies on temporal smoothing and model-based state propagation and therefore exhibits inertia in the presence of abrupt capacity changes. Consequently, short-term deviations between the Kalman filter-based SOH estimates and the fuzzy logic-based ordering are expected during such transition phases.

For each pack pair, two metrics are calculated to compare both methods (Table 3). The first metric, agreement, measures the concordance of the pairwise ordering between both methods, quantified by $P_Y^{(\alpha,\beta)}$ and the difference in the SOH estimates, and is evaluated only at time points where $P_Y^{(\alpha,\beta)} \neq 0$. The second metric, coverage, quantifies the decision yield of the fuzzy-based method and is defined as the fraction of all time points for which the fuzzy-based method provides an unambiguous ordering ($P_Y^{(\alpha,\beta)} \neq 0$). In contrast to agreement, coverage does not assess ordinal alignment between both methods, but measures the method's ability to produce decisive outcomes under varying operating conditions.

High values for both metrics indicate a strong and meaningful concordance in the ordering of a given pack pair. This is particularly the case for the pairs (5,4), (2,1), (1,3), (5,3), and (5,1). The greatest

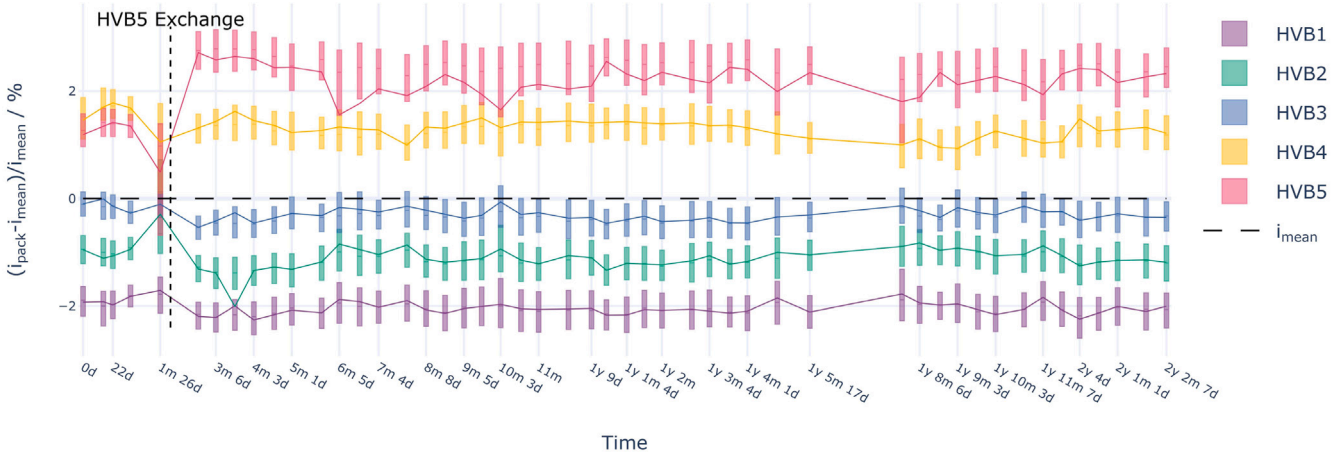

Fig. 6. Current distribution (D1) during high-current phases.

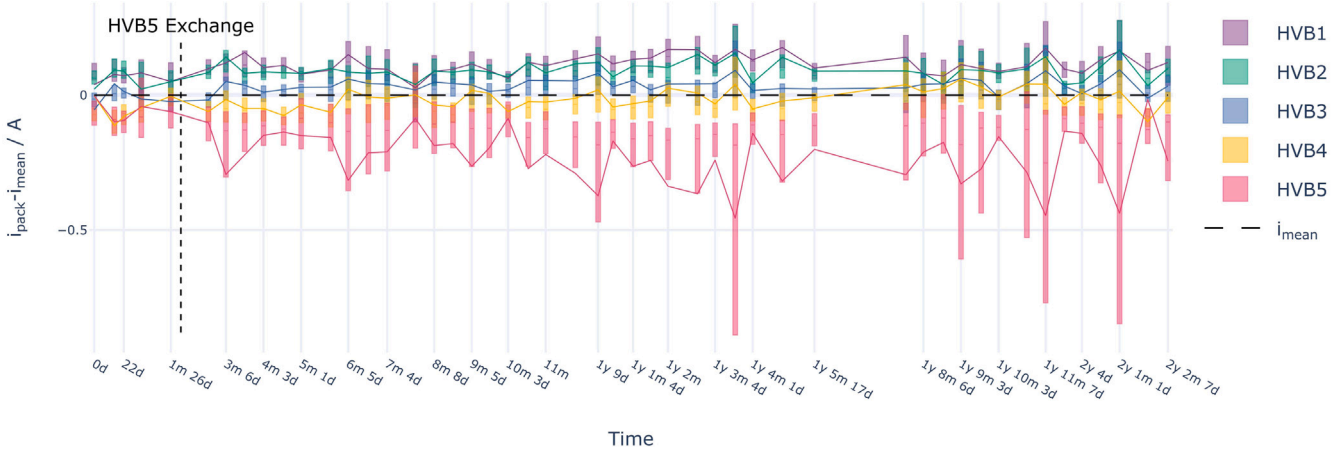

Fig. 7. Current distribution (D2) during low-current phases.

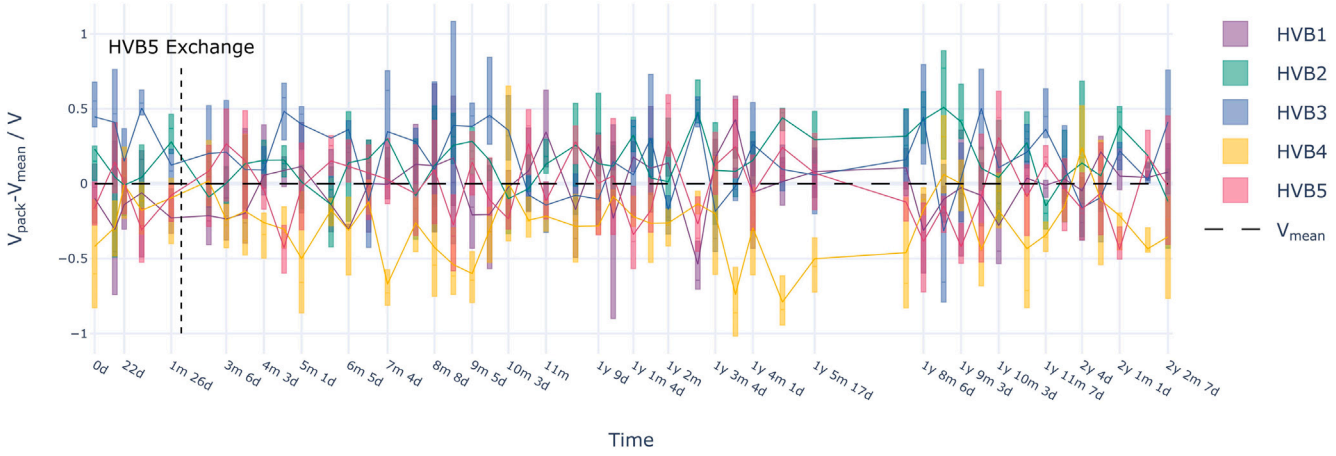

Fig. 8. Voltage distribution (D3) after disconnection from the DC link.

disagreement is observed for the pair (3,4), where the fuzzy logic–based method suggests a higher capacity for HVB 4, in contrast to the SOH estimates, which indicate the opposite relationship.

5. Discussion

The proposed method for estimating pairwise capacity differences offers significant advantages as a cross-check for SOH algorithms, but it is also subject to inherent limitations in its input assumptions and methodology. These aspects are discussed below, together with the application boundaries and the validation strategy.

5.1. Input-related limitations

The shape of the input distributions (D1)-(D3) is influenced by the observed load profile. Specifically, for distribution (D1), relevant

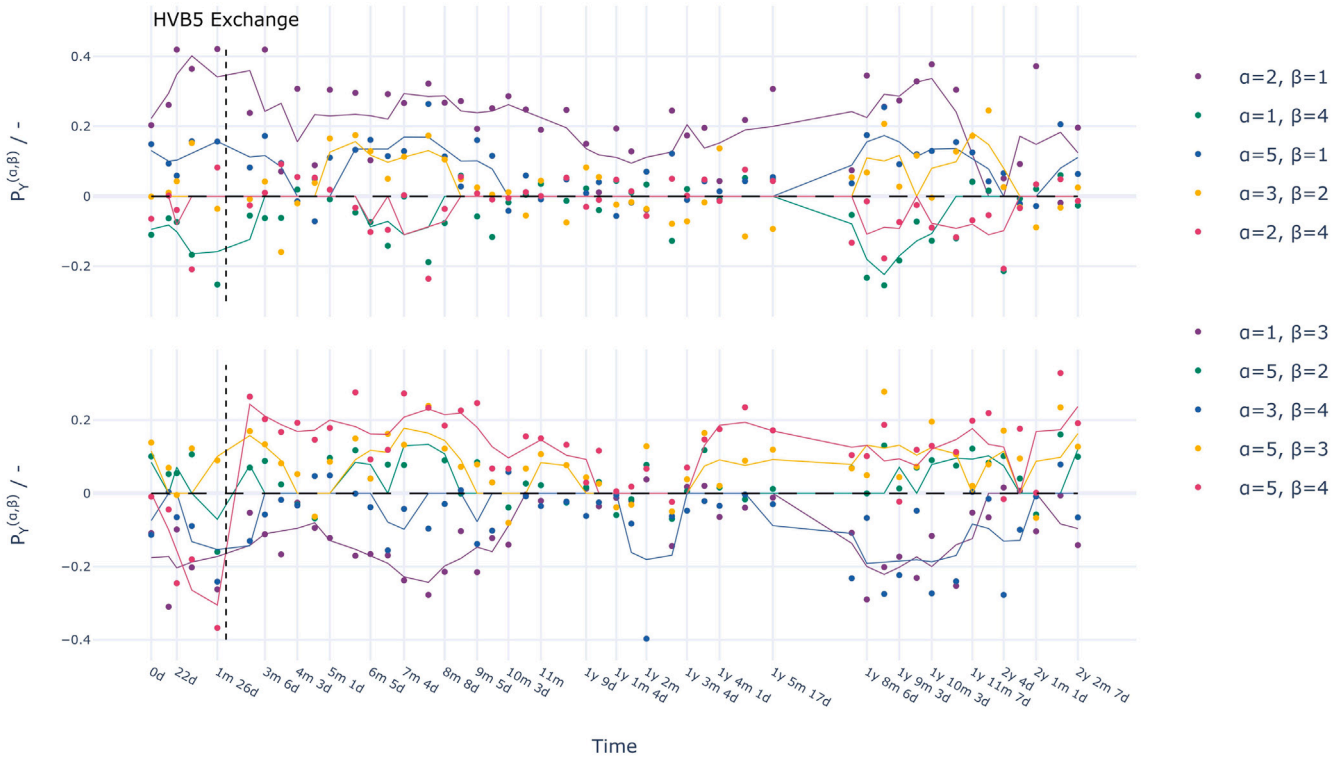

Fig. 9. $P_Y^{(\alpha,\beta)}$ for real-world data over the observed time period.

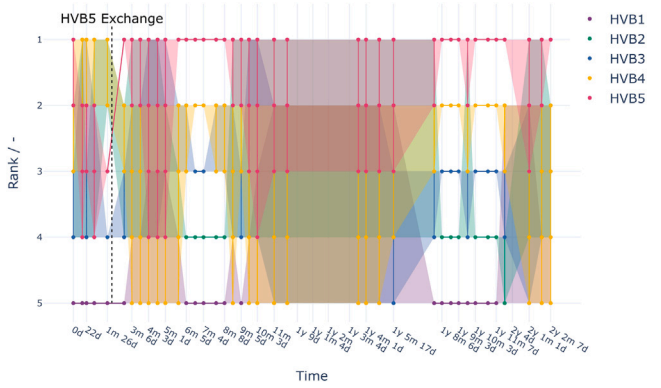

Fig. 10. Topological capacity ordering over the observed time period.

Table 3
Comparison of the pairwise capacity ordering derived from the Kalman filter-based estimates and the fuzzy logic-based results: agreement for non-zero outputs and coverage across all evaluated time points.

(α, β)	Agreement | $P_Y^{(\alpha,\beta)} \neq 0$	Coverage $P_Y^{(\alpha,\beta)} \neq 0$
(2, 1)	68.9%	95.7%
(1, 4)	62.5%	34.0%
(5, 1)	100.0%	55.3%
(3, 2)	100.0%	31.9%
(2, 4)	38.5%	27.7%
(1, 3)	100.0%	61.7%
(5, 2)	93.3%	31.9%
(3, 4)	4.5%	46.8%
(5, 3)	96.4%	59.6%
(5, 4)	97.4%	83.0%

factors are the temperature and SOC ranges during the high-current phases. The distributions (D2) and (D3) additionally depend on the temperature and SOC ranges encountered during low-current and rest phases, as well as on the transferred cumulated ampere-hours, since capacity recursively affects SOC and thus OCV differences. In the present approach, these effects are neglected, assuming they contribute randomly to the distributions and are therefore insignificant over the multi-day observation windows considered. While the analyzed data implicitly span diverse operating states, a systematic investigation under controlled SOC and temperature conditions could further clarify their impact on distributions (D1)-(D3) and is therefore considered future work.

The OCV-based distributions (D2) and (D3) further require sufficiently steep OCV-SOC gradients to provide meaningful information. Depending on the cell chemistry, monitoring may therefore need to be restricted to SOC regions where the OCV curve exhibits higher gradients. These distributions may also become distorted if the packs experience SOC offsets unrelated to capacity variations, which would translate into artificial OCV differences. In the present dataset, this effect is largely mitigated by typical overnight charging and subsequent rest periods, which allow pack SOCs to equilibrate. Occasional initial SOC mismatches at the start of a driving period are progressively diminished under extended load profiles, as the resulting SOC and OCV trajectories increasingly reflect the interaction of resistance-driven current redistribution and capacity differences rather than the initial offsets.

Additionally, extended periods in which packs remain continuously connected can partially equalize OCV via circulating currents, thereby reducing the information content of (D2) and (D3). The proposed method assumes that such operating phases do not dominate the dataset.

By definition, distribution (D1) reflects physical properties more directly than (D2) and (D3). Whereas variations in (D2) and (D3) accumulate gradually over time, differences in internal resistance are immediately apparent in (D1) during high-current phases. Consequently, (D1) may dominate the overall input, potentially biasing the analysis.

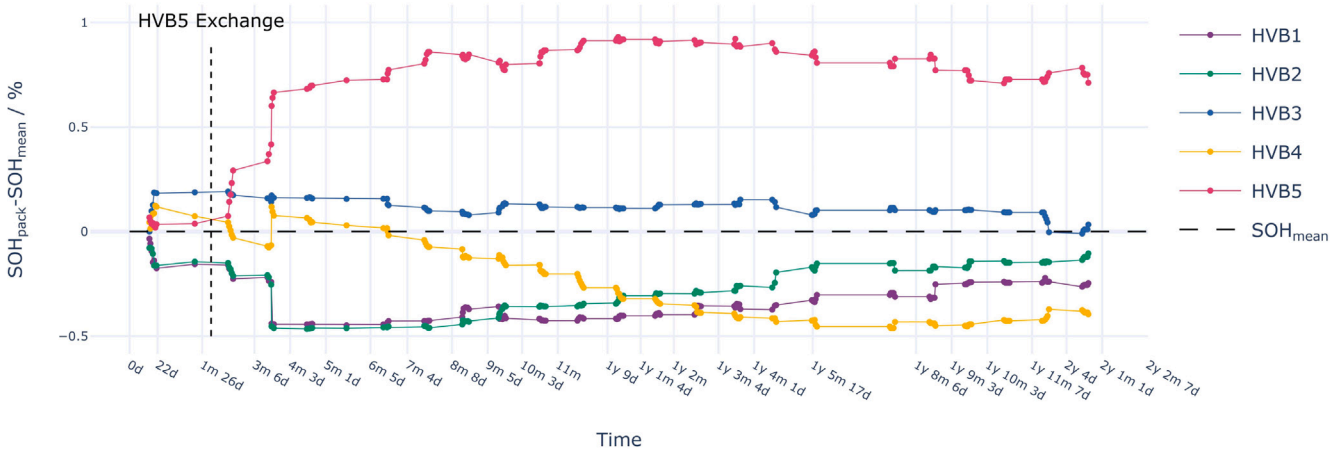

Fig. 11. Kalman filter-based SOH estimates over time.

This effect can be addressed by adjusting the percentage threshold that defines which operating periods qualify as high-current phases (Section 3) to balance the contributions of the different distributions, or, alternatively, by explicitly applying a different scaling to (D1) within the fuzzy rule calculations.

As the method relies on measurement signals, it is sensitive to sensor errors. Random noise can be mitigated by increasing the number of observed instances per distribution. Assuming N independent events per 7-day period, the standard error of the mean is $SE = \sigma_{tot}/\sqrt{N}$ with $\sigma_{tot} = \sqrt{\sigma_{data}^2 + \sigma_{sensor}^2}$, which allows estimating the probability of an incorrect sign attribution for the difference of two batteries (Eq. (19))

$$P_{sign,err} = \Phi\left(\frac{-|\Delta\mu| - \Delta b}{SE}\right) \tag{19}$$

$\Phi(\cdot)$ denotes the standard normal CDF, $\Delta\mu$ is the true distribution difference, and Δb is a relative bias. Observed differences from the real-world data (Section 4.2) and typical measurement uncertainties result in:

- **(D1)** $|i_{pack,mean}| \gtrsim 70$ A, $\Delta\mu \approx 0.7$–3.5 A. With $\sigma_{tot} \approx 0.6$–1.7 A and $N \approx 10^3$–$5 \cdot 10^3$, $SE \approx 0.02$–0.05 A, giving $P_{sign,err} \ll 1\%$.
- **(D2)** $|i_{pack,mean}| \lesssim 2$ A, $\Delta\mu \approx 0.1$–0.5 A. With $\sigma_{tot} \approx 0.2$–0.5 A and the same N, $SE \approx 0.005$–0.02 A, resulting again in $P_{sign,err} \ll 1\%$.
- **(D3)** Pack voltage differences up to $\Delta\mu \approx 1$ V. With $\sigma_{tot} \approx 0.2$–0.5 V and $N \approx 30$–100, the standard error is $SE \approx 0.02$–0.09 V, giving $P_{sign,err} \ll 1\%$.

The systematic relative bias Δb does not decrease with N and can dominate or distort the results if comparable to $|\Delta\mu|$. However, its influence decreases as the underlying capacity differences increase.

5.2. Methodological limitations

A positive correlation between internal resistance and capacity (i.e., the pack with higher internal resistance also exhibits the higher capacity) reduces the sensitivity of the proposed method. In this scenario, the current-imbalance-based SOC variation provides no counteracting indication, preventing unambiguous attribution of OCV differences to capacity variations. Instead, capacity differences simply contribute to larger observed variations in (D2) and (D3) than would be expected from internal-resistance-driven current imbalances alone. This mechanism provides a plausible explanation for the pronounced disagreement observed for pack pair (3,4) in Table 3. Here, distribution (D1) indicates a lower internal resistance for HVB 4, while the Kalman filter-based estimates suggest a lower capacity for the same pack. As a result, current-induced SOC effects reinforce the OCV trend, limiting the formation of a concessive inference point and thereby constraining the applicability of the proposed method. Comparable effects are observed for the pairs (1,4) and (2,4) later in the observation period, coinciding with the point at which the Kalman filter begins to indicate a reduced capacity for HVB 4.

Importantly, this behavior reflects a structural identifiability limitation of the proposed approach rather than random noise or insufficient data. When internal resistance and capacity variations act in the same direction, resistance-driven current redistribution and capacity-driven SOC evolution produce indistinguishable OCV trends, leaving no observational basis within the available voltage and current signals to disentangle their contributions. As a result, unambiguous pairwise ordering becomes fundamentally unattainable under such conditions. The fact that these disagreements emerge predominantly once the Kalman filter indicates a capacity decline of HVB 4 further suggests that this loss of sensitivity is conditional on increasing correlation between resistance and capacity effects, rather than a uniform limitation over the entire observation period.

Beyond this correlation-driven limitation, large internal resistance differences also introduce higher uncertainty. This is reflected, for example, in the comparison between pack pairs (5,4) and (5,1): although the Kalman filter-based estimates suggest a larger capacity difference between HVBs 5 and 1 than between HVBs 5 and 4, the proposed method provides more stable, non-zero outputs for (5,4). A plausible contributing factor is the larger internal resistance difference between HVBs 5 and 1, apparent in (D1), which reduces the likelihood of reaching the concessive point required for a confident inference. This highlights that the method is influenced not only by capacity differences but also by their interaction with resistance-induced current imbalances.

Taken together, the observed disagreements and delayed adaptations do not indicate methodological inconsistency but rather reflect fundamentally different sensitivities of the two approaches. While the Kalman filter prioritizes temporal consistency and model coherence, leading to delayed adaptation after abrupt changes, the fuzzy logic-based method reacts directly to emerging distributional patterns and relational evidence. Their divergence therefore highlights complementary strengths and failure modes, reinforcing the role of the proposed method as a plausibility-oriented cross-check rather than a replacement for model-based SOH estimation.

In general, the proposed reference capacity estimation provides only relative validation; thus, if the SOH algorithm is subject to a systematic bias affecting all battery packs equally, this method is unable to detect it.

As the reference is derived from accumulated operational data, its representativeness depends on the data amount and diversity. Therefore, the input distributions must be updated periodically as new data becomes available, with update intervals reflecting aging dynamics

rather than real-time requirements. In practice, such updates would align with the SOH evaluation frequency of the BMS. In its current form, the proposed method operates as a post-hoc analysis for existing SOH algorithms, without feeding back into the SOH estimation. As a next step, the method could be applied directly within an SOH algorithm to provide a real-time cross-check of estimated states and support corrective adjustments in the onboard BMS, thereby improving the SOH estimation at the source, which is considered a promising direction for future work.

The proposed method focuses on parallel-connected battery packs and does not resolve cell-level effects within series strings. This is acceptable since maintenance decisions are taken at the pack level. Moreover, in series-connected strings, all cells experience the same current, such that relative SOH differences are in principle observable via OCV-based monitoring, which is already well addressed in existing BMS cell monitoring and balancing strategies. In contrast, parallel-connected packs exhibit current redistribution driven by internal resistance and OCV differences, introducing an additional coupling effect. The proposed method specifically exploits this interaction and thus complements, rather than replaces, established cell-level diagnostics.

The effectiveness of the method further depends on the system topology. Its value increases with the number of parallel packs, as commonly the case in heavy-duty vehicle applications, where a larger set of pairwise comparisons enables mutual consistency checks and reduces ambiguity through logical cross-validation.

Situations in which multiple consistent orderings exist are explicitly interpreted as ambiguous. In the present formulation, no preference is applied between such orderings; instead, the resulting spread in ranks is treated as reduced confidence in the relative capacity comparison, avoiding over-interpretation of fuzzy outcomes. While not exploited further here, the degree of ordering ambiguity may itself carry diagnostic information. Systematically using the number or spread of consistent orderings as an additional monitoring indicator is therefore considered future work.

5.3. Application boundaries

The applicability and generalization of the proposed approach depend on a set of structural and operational conditions that define its domain of validity:

- *Parallel electrical coupling:* At least two battery packs must be electrically connected in parallel via sufficiently low-resistance paths, allowing measurable current redistribution between packs.
- *Dominant internal drivers and measurement consistency:* The current split must be primarily governed by pack-internal properties (internal resistance and OCV differences), rather than by peripheral effects such as unequal cabling, contact resistances, or external balancing hardware. Voltage and current measurements must be free of significant systematic inter-pack biases.
- *SOC reference alignment:* The energy management strategy must prevent persistent SOC offsets between packs that are unrelated to capacity differences, as such offsets would mask the characteristic OCV-SOC trajectories required for inference.
- *Informative operating conditions:* The available operational data must cover SOC and temperature ranges with sufficiently pronounced OCV-SOC gradients to provide meaningful information, which may restrict applicability depending on the cell chemistry.

5.4. Validation strategy and limitations

The validation presented in this study consists of three complementary components, designed to compensate for the absence of an absolute ground truth in the real-world data. First, the simulation results (Section 4.1) demonstrate the overall feasibility of the proposed methodology. Second, the relative capacity ranking from real-world data (Section 4.2) is compared with SOH estimates from a Kalman filter-based algorithm. Although this comparison does not constitute a formal validation, the generally high agreement between the two approaches indicates plausibility, with all pack capacities except HVB 4 consistently ranked. It also demonstrates an advantage of the fuzzy logic approach, which provides meaningful insights at early stages of battery usage, whereas conventional SOH algorithms typically require longer observation periods to stabilize. Third, a vehicle with one battery pack replaced by a new unit served as a reference scenario; the known capacity increase was correctly detected, confirming the method's practical applicability.

A conclusive validation using real-world fleet data, with ground truth measurements at multiple time points, has substantial practical challenges, as it requires close cooperation with the customer and battery removal from the vehicle for a standardized capacity measurement on a test bench, resulting in significant vehicle downtime.

6. Conclusion

In this work, a probabilistic method is introduced for ranking the capacities, and thus the SOHs, of parallel-connected battery packs. The proposed approach relies exclusively on measured pack-level voltage and current distributions and combines fuzzy logic-based pairwise comparisons with topological ordering to infer a global capacity ranking. This ranking provides an algorithm-independent plausibility reference for SOH estimation without requiring absolute capacity knowledge or detailed battery models, thereby addressing common practical limitations of conventional SOH assessment methods.

Simulation studies confirm the general feasibility of the approach. Field data from an electric city bus with five battery packs were analyzed over 26 months and evaluated using two complementary strategies: the replacement of one pack with a new unit, which provided a known relative capacity change, and a comparison against a Kalman filter-based SOH estimator. Across both references, the proposed method exhibited a high degree of consistency and correctly identified the replaced pack as having the highest capacity, highlighting its potential to improve the reliability and interpretability of SOH determinations in practical applications.

The method is inherently subject to several assumptions and limitations, which were explicitly discussed. Its effectiveness depends on sufficiently informative operating conditions, balanced SOC references, and the dominance of internal pack properties over external system effects. Furthermore, estimation sensitivity is reduced in scenarios where internal resistance and capacity differences are positively correlated, where resistance differences are large, or where systematic biases affect all packs equally. As a result, the method constitutes a relative, pack-level plausibility check rather than an absolute SOH estimator. Within its domain of validity, the proposed approach complements existing BMS-based SOH algorithms by providing an independent proxy ground truth that exploits current redistribution effects unique to parallel-connected systems.

Beyond the results presented in this work, several directions for future research and application have been identified. In particular, a systematic investigation of the influence of operating conditions such as temperature, SOC ranges, and load profiles could further refine the interpretation of the underlying input distributions, while the explicit use of ordering ambiguity itself may serve as an additional diagnostic indicator. Moreover, while the proposed method is currently applied as a post-hoc plausibility reference, its integration into onboard BMS algorithms represents a promising long-term perspective, enabling real-time consistency checks of SOH estimates and corrective adjustments directly within the BMS.

CRediT authorship contribution statement

Susann Wunsch: Writing – original draft, Visualization, Validation, Software, Methodology, Investigation, Conceptualization. **Natalia A. Cañas:** Writing – review & editing. **Eric Sax:** Writing – review & editing, Supervision.

Declaration of competing interest

The authors declare the following financial interests/personal relationships which may be considered as potential competing interests: Susann Wunsch and Natalia A. Cañas have patent #DE102025154163.9 pending to Daimler Truck AG (Daimler Buses GmbH). If there are other authors, they declare that they have no known competing financial interests or personal relationships that could have appeared to influence the work reported in this paper.

Acknowledgments

The authors would like to thank Alexis Kalk and Daniel Schall from the electrotechnical institute (ETI), Karlsruhe Institute of Technology (KIT), for their prompt support in providing the Kalman filter-based capacity estimates based on the provided measurement data. Their assistance supplied valuable additional data that helped to complete the analysis presented in this work.

Data availability

The authors do not have permission to share data.

References

[1] N. Kirkaldy, M.A. Samieian, G.J. Offer, M. Marinescu, Y. Patel, Lithium-ion battery degradation: Comprehensive cycle ageing data and analysis for commercial 21700 cells, J. Power Sources 603 (2024) 234185, http://dx.doi.org/10.1016/j.jpowsour.2024.234185, URL https://www.sciencedirect.com/science/article/pii/S0378775324001368.

[2] J. Vetter, P. Novák, M. Wagner, C. Veit, K.-C. Möller, J. Besenhard, M. Winter, M. Wohlfahrt-Mehrens, C. Vogler, A. Hammouche, Ageing mechanisms in lithium-ion batteries, J. Power Sources 147 (1) (2005) 269–281, http://dx.doi.org/10.1016/j.jpowsour.2005.01.006, URL https://www.sciencedirect.com/science/article/pii/S0378775305000832.

[3] M.B. Pinson, M.Z. Bazant, Theory of SEI formation in rechargeable batteries: capacity fade, accelerated aging and lifetime prediction, J. Electrochem. Soc. 160 (2) (2012) A243, http://dx.doi.org/10.1149/2.044302jes.

[4] J. Guo, Y. Li, K. Pedersen, D.-I. Stroe, Lithium-ion battery operation, degradation, and aging mechanism in electric vehicles: An overview, Energies 14 (17) (2021) http://dx.doi.org/10.3390/en14175220, URL https://www.mdpi.com/1996-1073/14/17/5220.

[5] G.L. Plett, Dual and joint EKF for simultaneous SOC and SOH estimation, in: Proceedings of the 21st Electric Vehicle Symposium (EVS21), Monaco, 2005, pp. 1–12.

[6] G.L. Plett, Sigma-point Kalman filtering for battery management systems of lipb-based HEV battery packs: Part 2: Simultaneous state and parameter estimation, J. Power Sources 161 (2) (2006) 1369–1384, http://dx.doi.org/10.1016/j.jpowsour.2006.06.004, URL https://www.sciencedirect.com/science/article/pii/S0378775306011438.

[7] D. Andre, C. Appel, T. Soczka-Guth, D.U. Sauer, Advanced mathematical methods of SOC and SOH estimation for lithium-ion batteries, J. Power Sources 224 (2013) 20–27, http://dx.doi.org/10.1016/j.jpowsour.2012.10.001, URL https://www.sciencedirect.com/science/article/pii/S0378775312015303.

[8] H.M. Fahmy, H.M. Hasanien, I. Alsaleh, H. Ji, A. Alassaf, State of health estimation of lithium-ion battery using dual adaptive unscented Kalman filter and Coulomb counting approach, J. Energy Storage 88 (2024) 111557, http://dx.doi.org/10.1016/j.est.2024.111557, URL https://www.sciencedirect.com/science/article/pii/S2352152X24011423.

[9] H. Lee, C. Casten, H.K. Fathy, State estimation for parallel-connected batteries via inverse dynamic modeling, J. Energy Storage 118 (2025) 116025, http://dx.doi.org/10.1016/j.est.2025.116025, URL https://www.sciencedirect.com/science/article/pii/S2352152X25007388.

[10] D. Zhang, L.D. Couto, S. Benjamin, W. Zeng, D.F. Coutinho, S.J. Moura, State of charge estimation of parallel connected battery cells via descriptor system theory, in: 2020 American Control Conference, ACC, 2020, pp. 2207–2212, http://dx.doi.org/10.23919/ACC45564.2020.9147284.

[11] L. Wang, Y. Xu, E. Wang, X. Zhao, S. Qiao, G. Li, H. Sun, Modeling and state of charge estimation of inconsistent parallel lithium-ion battery module, J. Energy Storage 51 (2022) 104565, http://dx.doi.org/10.1016/j.est.2022.104565, URL https://www.sciencedirect.com/science/article/pii/S2352152X22005825.

[12] L. Wang, J. Ma, X. Zhao, X. Li, K. Zhang, Online estimation of state-of-charge inconsistency for lithium-ion battery based on SVSF-VBL, J. Energy Storage 67 (2023) 107657, http://dx.doi.org/10.1016/j.est.2023.107657, URL https://www.sciencedirect.com/science/article/pii/S2352152X2301054X.

[13] Y. Che, A. Foley, M. El-Gindy, X. Lin, X. Hu, M. Pecht, Joint estimation of inconsistency and state of health for series battery packs, Automot. Innov. 4 (2021) 103–116, http://dx.doi.org/10.1007/s42154-020-00128-8, URL https://link.springer.com/article/10.1007/s42154-020-00128-8.

[14] S. Peng, Y. Miao, R. Xiong, J. Bai, M. Cheng, M. Pecht, State of charge estimation for a parallel battery pack jointly by fuzzy-PI model regulator and adaptive unscented Kalman filter, Appl. Energy 360 (2024) 122807, http://dx.doi.org/10.1016/j.apenergy.2024.122807, URL https://www.sciencedirect.com/science/article/pii/S0306261924001909.

[15] A. Zenati, P. Desprez, H. Razik, S. Rael, A methodology to assess the state of health of lithium-ion batteries based on the battery's parameters and a fuzzy logic system, in: 2012 IEEE International Electric Vehicle Conference, 2012, pp. 1–6, http://dx.doi.org/10.1109/IEVC.2012.6183268.

[16] D. Saji, P.S. Babu, K. Ilango, Soc estimation of lithium ion battery using combined Coulomb counting and fuzzy logic method, in: 2019 4th International Conference on Recent Trends on Electronics, Information, Communication and Technology, RTEICT, 2019, pp. 948–952, http://dx.doi.org/10.1109/RTEICT46194.2019.9016956.

[17] M. Stang, M. Sommer, D. Baumann, Y. Zijia, E. Sax, Adaptive customized forward collision warning system through driver monitoring, in: 2020 Future Technologies Conference, FTC, 2020, pp. 757–772, http://dx.doi.org/10.1007/978-3-030-63089-8_50.

[18] M. Woźniak, A. Zielonka, A. Sikora, Driving support by type-2 fuzzy logic control model, Expert Syst. Appl. 207 (2022) 117798, http://dx.doi.org/10.1016/j.eswa.2022.117798, URL https://www.sciencedirect.com/science/article/pii/S0957417422010636.

[19] M. Dubarry, N. Vuillaume, B.Y. Liaw, Origins and accommodation of cell variations in li-ion battery pack modeling, Int. J. Energy Res. 34 (2) (2010) 216–231, http://dx.doi.org/10.1002/er.1668, URL https://onlinelibrary.wiley.com/doi/10.1002/er.1668.

[20] Y. Zheng, M. Ouyang, L. Lu, J. Li, Understanding aging mechanisms in lithium-ion battery packs: From cell capacity loss to pack capacity evolution, J. Power Sources 278 (2015) 287–295, http://dx.doi.org/10.1016/j.jpowsour.2014.12.105, URL https://www.sciencedirect.com/science/article/pii/S0378775314021338.

[21] S.F. Schuster, M.J. Brand, P. Berg, M. Gleissenberger, A. Jossen, Lithium-ion cell-to-cell variation during battery electric vehicle operation, J. Power Sources 297 (2015) 242–251, http://dx.doi.org/10.1016/j.jpowsour.2015.08.001, URL https://www.sciencedirect.com/science/article/pii/S0378775315301555.

[22] M. Baumann, L. Wildfeuer, S. Rohr, M. Lienkamp, Parameter variations within li-ion battery packs – theoretical investigations and experimental quantification, J. Energy Storage 18 (2018) 295–307, http://dx.doi.org/10.1016/j.est.2018.04.031, URL https://www.sciencedirect.com/science/article/pii/S2352152X18300732.

[23] E. Hosseinzadeh, S. Arias, M. Krishna, D. Worwood, A. Barai, D. Widanalage, J. Marco, Quantifying cell-to-cell variations of a parallel battery module for different pack configurations, Appl. Energy 282 (2021) 115859, http://dx.doi.org/10.1016/j.apenergy.2020.115859, URL https://www.sciencedirect.com/science/article/pii/S0306261920313337.

[24] S. Wunsch, N.A. Cañas, C. Rivas-Zöller, E. Sax, Introducing a comprehensive state of health inconsistency (SOHI) as novel parameter to describe and monitor the aging state variance of connected batteries, E-Prime - Adv. Electr. Eng. Electron. Energy 13 (2025) 101077, http://dx.doi.org/10.1016/j.prime.2025.101077, URL https://www.sciencedirect.com/science/article/pii/S2772671125001846.